Magnetic Cr doping of Bi_2Se_3: Evidence for divalent Cr from x-ray spectroscopy

A. I. Figueroa,[1] G. van der Laan,[1] L. J. Collins-McIntyre,[2] S.-L. Zhang,[2] A. A. Baker,[1,2] S. E. Harrison,[2,3] P. Schönherr,[2] G. Cibin,[4] and T. Hesjedal[2,4]

[1]*Magnetic Spectroscopy Group, Diamond Light Source, Didcot, OX11 0DE, United Kingdom*

[2]*Department of Physics, Clarendon Laboratory, University of Oxford, Oxford, OX1 3PU, United Kingdom*

[3]*Department of Electrical Engineering, Stanford University, Stanford, California 94305, USA*

[4]*Diamond Light Source, Didcot, OX11 0DE, United Kingdom*

(Received 1 August 2014; revised manuscript received 19 September 2014; published 3 October 2014)

Ferromagnetically doped topological insulators with broken time-reversal symmetry are a prerequisite for observing the quantum anomalous Hall effect. Cr-doped $(Bi,Sb)_2(Se,Te)_3$ is the most successful materials system so far, as it combines ferromagnetic ordering with acceptable levels of additional bulk doping. Here, we report a study of the local electronic structure of Cr dopants in epitaxially grown Bi_2Se_3 thin films. Contrary to the established view that the Cr dopant is trivalent because it substitutionally replaces Bi^{3+}, we find instead that Cr is divalent. This is evidenced by the energy positions of the Cr K and $L_{2,3}$ absorption edges relative to reference samples. The extended x-ray absorption fine structure at the K edge shows that the Cr dopants substitute on octahedral sites with the surrounding Se ions contracted by $\Delta d = -0.36$ Å, in agreement with recent band structure calculations. Comparison of the Cr $L_{2,3}$ x-ray magnetic circular dichroism at $T = 5$ K with multiplet calculations gives a spin moment of 3.64 μ_B/Cr_{bulk}, which is close to the saturation moment for Cr^{2+} d^4. The reduced Cr oxidation state in doped Bi_2Se_3 is ascribed to the formation of a covalent bond between Cr $d(e_g)$ and Se p orbitals, which is favored by the contraction of the Cr-Se distances.

DOI: 10.1103/PhysRevB.90.134402 PACS number(s): 75.30.Hx, 78.70.Dm, 75.50.Pp, 73.61.Ng

I. INTRODUCTION

The class of materials with tetradymite structure, including Bi_2Te_3, Bi_2Se_3, and Sb_2Te_3, has been extensively studied for thermoelectric applications [1] and more recently attracted profound interest as three-dimensional topological insulators (TIs) [2]. These materials, which also occur naturally as vein minerals [3], can be grown as high purity samples in the form of single crystals [4], epitaxial films [5], and nanostructures [6].

Magnetic TIs are the prerequisite for observing the quantum anomalous Hall (QAH) effect [7] and other exotic magnetoelectric effects [8]. In these materials, ferromagnetic ordering leads to the breaking of time-reversal symmetry (TRS) and the opening of a band gap around the Dirac point [8–10]. The QAH effect has been experimentally demonstrated in Cr-doped $(Bi,Sb)_2Te_3$ [11], and is predicted to exist in other Cr-doped dichalcogenides such as $Bi_2(Se,Te)_3$ as well [12]. The choice of Cr as dopant for dichalcogenides over the obvious transition metals Mn [13] and Fe [14] is determined by the electronic structure. Whereas Mn and Fe lead to a quasimetallic state [15], Cr gives a gapped ferromagnetic ground state in, e.g., Bi_2Se_3, as it is believed to be in a trivalent state which is isoelectronic to Bi^{3+} [7,16]. Other than $(Bi_{1-x}Cr_x)_2Se_3$, with substitutional Cr on Bi sites, a possible doping scenario might be the incorporation of Cr in the van der Waals gap, $Cr_yBi_2Se_3$, which gives a lower oxidation state with increased n-type carrier concentration and increased c lattice spacing (see Fig. 1).

The established opinion in the literature is that the Cr dopant is trivalent because it substitutionally replaces the Bi^{3+} in Bi_2Se_3 similar to related compounds [7,11,15–23]. In this paper, we use the element-specific techniques of extended x-ray absorption fine structure (EXAFS), x-ray absorption spectroscopy (XAS), and x-ray magnetic circular dichroism (XMCD) to determine the local electronic and magnetic state of the Cr dopants in Bi_2Se_3. Contrary to the prevalent belief we find that the substitutional Cr is mainly divalent, which is due to the covalent character of the Cr–Se bonds.

II. VALENCE STATE OF Cr IN Bi_2Se_3

The assignment of the oxidation state of Cr has been based on various results, namely theoretical methods such as band structure calculations or experimental techniques such as transport measurements, magnetometry, and core-level spectroscopies. Below, we will discuss the status of these different methods and make some relevant comments.

A. Band structure calculations.

Larson and Lambrecht [17] calculated substitutionally doped transition metals in Bi_2Te_3, Bi_2Se_3, and Sb_2Te_3 using the full-potential linearized muffin-tin orbital method in local spin-density approximation (LSDA). These authors obtained an oxidation state of 3+ for the early first row transition-metal series up to Fe, which in the latter part reduces closer to 2+ (Co) or 1+ (Ni). This was ascribed to the hybridization between the transition metal 3d and Se/Te p states. These results were confirmed and extended using first principle calculations in the generalized gradient approximation (GGA) by Zhang *et al.* [15,24], who found that Cr^{3+} in Bi_2Se_3 has a negative formation energy for the whole range of chemical potential, indicating the doping of Cr can occur spontaneously.

It is worth noting that density functional theory (DFT) calculations underestimate the 3d electron correlation effects and exchange interaction. In DFT the ground state is expressed as a function of electron density. In its practical application, called the local density functional approach (LDA), the kinetic, nuclear, and Hartree potentials are taken into account with exchange and correlation effects described by a combined potential. The potentials are local functions of the electron

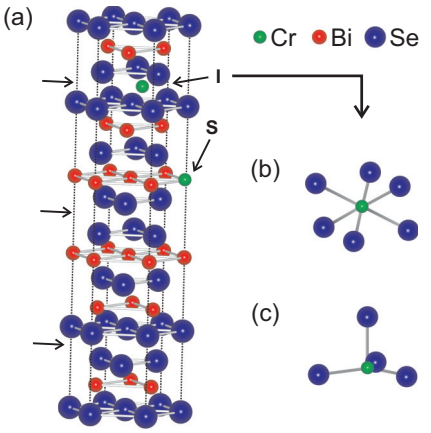

FIG. 1. (Color online) (a) Crystal structure of Cr-doped Bi_2Se_3. Quintuple layers (Se-Bi-Se-Bi-Se) are separated by a weakly bonding van der Waals gap as indicated by arrows. Cr dopants are shown substituting for Bi (S) and interstitially in the van der Waals gap (I). The interstitial Cr is shown in (b) distorted octahedral and (c) distorted tetrahedral coordination.

density and any complications are collected in the exchange-correlation potential. Such calculations have been very successful in obtaining the exact ground state energy and charge density, taking into account the effective electron correlation; however, the wave function in the LDA approximation has no physical significance and should only be used at the Fermi level.

B. Transport measurements.

Indirect insight into the oxidation state of the dopant can be obtained from transport measurements via the determination of the carrier concentration and supporting models.

Kou *et al.* [20] argued that given the intrinsic *n*-type behavior caused by Se vacancies in undoped Bi_2Se_3 thin films, the suppression of electron concentration in $(Bi_{1-x}Cr_x)_2Se_3$ means that the majority of the Cr dopants are incorporated within the crystal lattice in the form of Cr^{3+}, and therefore substitute on the Bi sublattice. Also in the diluted magnetic semiconductor $Sb_{2-x}Cr_xTe_3$ transport measurements suggest that Cr is 3+ and replaces Sb [25]. Hence isoelectronic substitution of Cr^{3+} for Bi (or Sb) gives a rather weak charge carrier (hole) dependence on the Cr content, while Cr^{2+} means a source of carrier doping.

We note that the above argument does not take into account that Bi^{3+} refers merely to a formal designation for the Bi–Se bonding in Bi_2Se_3, which is not necessarily purely ionic but can also be covalent. Furthermore, Cr^{3+} has a very different ionic radius than Bi^{3+} (see Table I). Substitution of Cr with its smaller radius leads to a displacement of the neighboring Se atoms, which can enhance the covalency of the chemical bonds [15,17]. In the case of a covalent bond, or resonant valence bond, such as Cr^{3+}–$Se^{2-} \leftrightarrow Cr^{2+}$–$Se^{1-}$, the charge is redistributed locally over the bond atoms, so it does not become a free carrier taking part in charge transport.

C. Magnetometry.

So far, evidence from conventional magnetometry is inconclusive. Magnetic studies on epitaxial, Cr-doped Bi_2Se_3 thin films using superconducting quantum interference device (SQUID) magnetometry [19] and polarized neutron reflectometry studies [26] consistently reported a magnetic moment of $\sim 2\,\mu_B$/Cr. Such a value is much less than the Hund's rule value of $3\,\mu_B$ for the spin moment of substitutional Cr^{3+} in Bi sites. It would agree with low-spin Cr^{4+}, which requires an octahedral crystal field above 2.5 eV [27], which is an unlikely scenario because the energy to overcome the exchange interaction is very high. First-principles calculations for Cr adatoms on the surface of Bi_2Se_3 give moments of $\sim 3.78\,\mu_B$ for substitutional Cr and $\sim 0.71\,\mu_B$ for interstitial Cr [28].

TABLE I. Crystal ionic radii for sixfold coordinated Cr, Bi, Sb cations and for Se, Te anions (Ref. [29]).

Ion	Crystal ionic radius (pm)
Cr^{2+} (high spin)	94
Cr^{2+} (low spin)	87
Cr^{3+}	75.5
Cr^{4+}	69
Cr^{5+}	63
Bi^{3+}	117
Sb^{3+}	90
Se^{2-}	184
Te^{2-}	207

D. Core-level spectroscopy.

The most direct way to determine the local electronic structure of 3*d* transition metal atoms is using XAS and XMCD as valence-, site-, and symmetry-selective probe [27,30–32], where the sum rules can be used to extract spin and orbital moments [33,34]. Unfortunately, the case of Cr is less clear cut than that of Mn, Fe, Co, or Ni, because of the smaller energy separation between the L_3 and L_2 manifolds and also because experimental case studies for Cr are more scarce. The Cr $L_{2,3}$ XAS and XMCD of ionic Cr^{3+}, as observed for $CrFe_2O_4$ [35] and Cr-doped Fe_3O_4 [36,37], show a sharp multiplet structure. Comparable XAS and XMCD structures have been reported by Kimura *et al.* [38] for Cr in the bulk of the ferromagnetic spinel-type chalcogenides, $CdCr_2Se_4$, $CuCr_2S_4$, and $CuCr_2Sr_4$, from which the authors concluded Cr^{3+}. Yaji *et al.* [39] reported XMCD of ferromagnetic chromium tellurides, Cr_5Te_6 and Cr_2Te_3, from which they concluded $Cr^{4.5+}$. The XAS and XMCD of $Zn_{1-x}Cr_xTe$ was ascribed to Cr^{2+} [40]. In the diluted magnetic semiconductor, Cr-doped Ga_2Se_3/Si(001), the Cr valence state was assigned as being 3+ [18]. Hence the existing literature on XAS and XMCD provides a rather limited guidance to solve the valence issue of Cr-doped Bi_2Se_3.

E. Purpose of the study.

It is our aim to present convincing evidence that the Cr dopants in Bi_2Se_3 are not purely 3+, but instead have mainly 2+ character, arising from a covalent Cr–Se bond. The rationale behind this unconventional result is based on several considerations. Bi_2Se_3 grows *n* type [41,42], however, this is of no importance when trying to understand the magnetic properties of doped TIs, since—contrary to, e.g.,

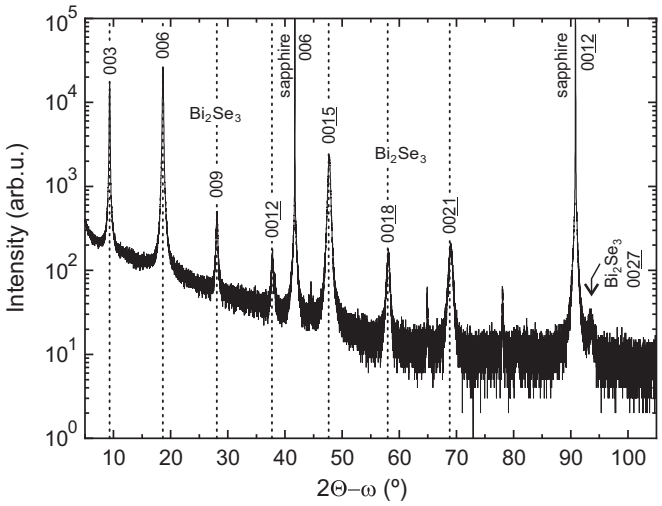

FIG. 2. X-ray diffraction of the ∼100-nm-thick Cr-doped Bi_2Se_3 film on *c*-plane sapphire. The dotted lines represent the positions of the (003$\underline{l}$) family of diffraction peaks for undoped Bi_2Se_3.

diluted magnetic semiconductors [43]—the magnetic state is not determined by the carrier concentration but in fact by the chemical bonds of the dopants [44].

For the light transition metals, the first Hund's rule gives a large energy stabilization for the high-spin state due to the exchange interaction. In Bi_2Te_3 and Sb_2Te_3, DFT calculations predict the Cr dopant to be trivalent with only weak hybridization between the Cr *d* and Te *p* states [17]. However, in Bi_2Se_3 the Se *p* state is closer to the Fermi level, enabling a stronger hybridization with the Cr 3*d* state (see, e.g., Fig. 2 in Ref. [17]). In a cubic crystal field the Cr 3*d* states are split into t_{2g} and e_g states. In an octahedral site, e_g orbitals are directed towards the anions, while t_{2g} orbitals are pointing between the anions, which gives a lower energy. The large exchange interaction splits the crystal-field states into spin-up and spin-down bands, which gives $t_{2g}^{3\uparrow}$ and $t_{2g}^{3\uparrow}e_g^{1\uparrow}$ configurations for Cr^{3+} and Cr^{2+}, respectively. The occupied Se *p* states just below the Fermi level hybridize with the unoccupied Cr e_g states just above the Fermi level. This reduces the amount of charge transfer across these two atoms, and enhances the Cr^{2+} character. The situation will be different for Sb_2Te_3 or Bi_2Te_3, where Cr tends more towards 3+, as caused by differences in crystal ionic radii and position of the anion *p* band with respect to the Fermi level.

Upon substitution the Cr atom replaces Bi^{3+} which is located between Se atoms. The neighboring Se atoms move to accommodate the smaller radius of the Cr atom, resulting in a local relaxation of the lattice parameters, while the remaining atoms undergo a much smaller change and maintain the original crystal structure [17,45].

III. EXPERIMENTAL TECHNIQUES

A. Sample growth and characterization

Growth and composition. Cr-doped Bi_2Se_3 thin film samples have been grown by molecular beam epitaxy (MBE) on *c*-plane sapphire. First, a 20-nm-thick Bi_2Se_3 buffer layer is deposited at 250 °C, before the Cr-doped film is grown at 300 °C. Rutherford backscattering (RBS) results showed that the investigated film had a thickness of ∼100 nm and contained 4.6 at.% Cr, 35.4 at.% Bi, and 60.0 at.% Se (for all values the error is ±0.5 at.%) [26]. The Se concentration of 60% confirms substitutional Cr incorporation on a Bi site (see Fig. 1). The obtained composition agrees with the oxidation states of Cr^{3+}, Bi^{3+}, and Se^{2-}, fulfilling an overall charge neutrality. It equally agrees with the case that the sample contains charge-neutral clusters where the electrons are redistributed between the central Cr and its neighboring Se atoms as $Cr^{3+}Se_x^{2-} \rightarrow Cr^{(3-\delta)+}Se_x^{(2-\delta/x)-}$. Hence there is no requirement to have Cr^{3+}.

XRD. X-ray diffraction (XRD) and rocking curves show high structural quality without any parasitic phases as seen in Fig. 2; for further details see Ref. [26]. The determined *c*-axis lattice parameter is 28.65 Å, compared to 28.66 Å for undoped films (ICSD 617072: 28.636 Å for Bi_2Se_3) [26]. Contrary to the report by Haazen *et al.* [19] an expansion of the *c*-axis lattice constant was not observed, also supporting the substitutional incorporation of Cr.

Electric properties. The electric properties of the Cr-doped film were measured at temperatures down to 5 K in a field of ±500 mT at which the ferromagnetic system is in saturation. Measurements were done in a physical property measuring system (PPMS) on a sample measuring 5×5 mm^2 with indium contacts using the van der Pauw geometry. The film is *n* type and at 5 K the resistivity is $\rho = 1.58$ mΩ cm, the mobility $\mu = 124$ cm^2 V^{-1} s^{-1}, and the sheet carrier density $n = -3.16\times10^{19}$ cm^{-3}, which is a typical value for dilute magnetic semiconductors [46]. The two-dimensional carrier concentration is with -3.78×10^{14} cm^{-2} almost an order of magnitude higher than a similar Cr-doped $(Bi_xSb_{1-x})_2Te_3$ thin film of six quintuple layer thickness (2.2×10^{13} cm^{-2} at 1.9 K) [22], which can be attributed to the much reduced bulk carrier contribution in the ultrathin film limit. Compared to Cr-doped bulk crystals ($Cr_{0.2}Bi_{0.36}Sb_{1.44}Te_3$, $p = 1.45\times10^{20}$ cm^{-3} at 2 K); however, the measured carrier concentration is about an order of magnitude smaller [47].

Magnetization measurements. The magnetization loop measured by SQUID is dominated by a ferromagnetic open loop with a coercive field of ∼10 mT at 3 K and a T_C of 12.5 K (not shown here; see Ref. [26]).

B. X-ray absorption fine structure

Instrumental. X-ray absorption near edge structure (XANES) and EXAFS at the Cr *K* edge (5989 eV) were measured at room temperature on beamline B18 at the Diamond Light Source to characterize the electronic and structural environment of the Cr atoms. A nine-element solid-state Ge detector with digital signal processing for fluorescence XAS, high energy resolution, and high count rate was used to measure with the beam at 45° incidence with respect to the sample plane. All spectra were acquired in quick-EXAFS mode using the Pt-coated branch of collimating and focusing mirrors, a Si(111) double-crystal monochromator and a pair of harmonic rejection mirrors. The energy range for each scan allowed us to extract information in the extended region up to $k = (12–14)$ $Å^{-1}$. Polycrystalline samples of CrSe, Cr_2O_3, and CrO_3 in powder form, and a Cr foil of 5 μm in thickness were measured as references in transmission detection mode.

EXAFS analysis. EXAFS spectra were processed and analyzed using different tools of the IFFEFIT XAS package [48]. This involved preliminary reduction of the EXAFS raw data, background removal of the x-ray absorption data $\mu(E)$, conversion of $\mu(E)$ to $\chi(k)$, normalization and weighting scheme, all of them performed with AUTOBK and ATHENA. EXAFS data analysis and fitting on all references and samples were performed in ARTEMIS, making use of models based on crystallographic information found in the ICSD database. The atomic clusters used to generate the scattering paths for fitting were generated with ATOMS [49].

C. X-ray magnetic circular dichroism

Instrumental. XMCD was used to probe the local electronic character of the electronic and magnetic ground state of the Cr dopants [31]. This technique has previously provided an unambiguous determination of the ground state of transition-metal and rare-earth dopants in TIs [13,50–53]. The XAS at the Cr $L_{2,3}$ edges was simultaneously measured in total-electron yield (TEY) and fluorescence yield (FY) detection on beamline I10 (BLADE) at the Diamond Light Source at a temperature of 5 K using a 14 T superconducting magnet. The XMCD is obtained as the difference between the two XAS spectra recorded with the x-ray helicity vector and applied magnetic field antiparallel and parallel $(\mu^- - \mu^+)$. The measurements were performed by reversing the polarization of the incident x rays, to avoid switching the high field of the superconducting magnet. The samples (with the surface normal along the c axis) were measured both at normal and grazing incidence, with the magnetic field always along the x-ray beam. The degree of circular polarization in the energy region of interest is close to 100%. The area probed by the beam ($\sim 20\times 200\ \mu m^2$) is much smaller than the sample size ($10\times 10\ mm^2$).

D. Multiplet calculations and sum rules

Calculational. Atomic multiplet theory is used to calculate the electric-dipole transitions $3d^n \rightarrow 2p^5 3d^{n+1}$, where the spin-orbit and electrostatic interactions are treated on an equal footing [54,55]. The wave functions of the initial- and final-state configurations are calculated in intermediate coupling using Cowan's atomic Hartree-Fock (HF) code with relativistic corrections [30,56]. The atomic electrostatic interactions include the $2p$-$3d$ and $3d$-$3d$ Coulomb and exchange interactions, which are reduced to 70% of their atomic HF value to account for the intra-atomic screening [54]. Hybridization effects are included by mixing $3d^n$ with $3d^{n+1}\underline{L}$ configurations, where $\underline{L}$ represents an electron on the neighboring atoms in states of appropriate symmetry. The Cr L_3 (L_2) line spectra are broadened by a Lorentzian of $\Gamma = 0.3$ eV (0.4 eV) for intrinsic lifetime broadening and a Gaussian of $\sigma = 0.15$ eV for instrumental broadening.

Sum rule analysis. Sum rules relate the integrated intensities of the XAS and XMCD $L_{2,3}$ spectra to the orbital and spin magnetic moments as

$$m_L = -\frac{4}{3}\frac{q}{r}(10-n), \tag{1a}$$

$$m_S = -\frac{6p-4q}{r}(10-n)C - \langle T_z\rangle, \tag{1b}$$

where p is the integrated intensity of $(\mu^- - \mu^+)$ over the L_3 edge and q is that over the $L_{2,3}$ edges, r is the integrated intensity of $(\mu^- + \mu^+)$ over the $L_{2,3}$ edges (see Fig. 4), n is the number of $3d$ electrons, and $\langle T_z\rangle$ is the expectation value of the magnetic dipole operator [33,34,57].

While the sum rule for m_L is theoretically precise, the sum rule for m_S requires a correction factor C [see Eq. (1b)]. Since the integrals are taken separately over the two edges, C takes into account the jj mixing between the $2p_{3/2}$ and $2p_{1/2}$ manifolds. Its value can be obtained from multiplet calculations, by comparing the spin moment extracted from the sum rule analysis of the calculated $L_{2,3}$ spectra with the corresponding calculated ground state moment [58]. For the ground state of Cr using a range of different parameters for the crystal-field interaction and hybridization, we obtain $C = 2.0 \pm 0.2$, where the error bar reflects the parameter range.

IV. RESULTS AND DISCUSSION

A. X-ray absorption fine structure results

The normalized XANES at the Cr K edge of the Cr-doped Bi_2Se_3 thin film together with CrSe, Cr_2O_3, CrO_3, and Cr foil are plotted in Fig. 3(a). Direct comparison of the energy position of the absorption jump for the thin film with the references suggests that the Cr dopants in Bi_2Se_3 have an oxidation state close to that of the CrSe standard, which means Cr^{2+}. Furthermore, the Cr-doped sample displays no pre-edge peak characteristic of a tetrahedral (noncentrosymmetric) local environment, such as that observed in the CrO_3 spectrum. Hence we deduce that Cr is not tetrahedrally coordinated.

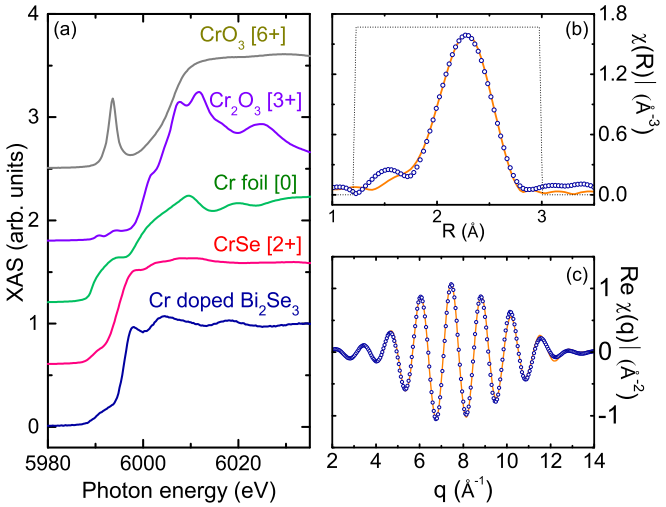

FIG. 3. (Color online) (a) Cr K edge XANES for Cr-doped Bi_2Se_3 thin film and comparison with CrSe, Cr_2O_3, CrO_3, and Cr foil for reference. The Cr oxidation state is indicated in the square brackets. Spectra have been shifted vertically for clarity. (b) Fourier transform of EXAFS signal at the Cr K edge on the thin film (symbols) together with the best fit to the first coordination shell (solid line). The dotted box gives the Kaiser-Bessel window function. (c) Contribution of the first coordination shell to the EXAFS signal (symbols) together with its best fit (solid line).

The structural analysis of the Cr-doped Bi_2Se_3 thin film that can be extracted from the $\chi(k)$ EXAFS signal is studied by the Fourier transform (FT), shown in Fig. 3(b), performed over a k range from 3.3 to 12 Å^{-1} using a k^2 weight, a $\Delta k = 1.5$ Å^{-1}, and a Kaiser-Bessel window function. Despite the high crystal quality of the Cr-doped Bi_2Se_3 thin film, possible angular variations of the EXAFS signal due to polarization of the beam are not significant to our analysis given the angular range these measurements have been performed (fluorescence at 45°). In this case, the EXAFS signal reflects an average of the in-plane and out-of-plane scattering paths in the sample, equivalent to measurements in polycrystalline samples.

Different models were tested to fit the EXAFS signal at the Cr K edge of the doped TI. Fits were performed on the R space in a range from 1.2 to 3 Å using a Kaiser-Bessel window function, so that it covered Cr in the first coordination shell [see Fig. 3(b) and its backwards FT in Fig. 3(c)]. The parameters fitted were the interatomic distance (R), the Debye-Waller factor (σ^2) for each scattering path, and a general shift in the threshold energy (ΔE_0). The amplitude reduction factor S_0^2 was set to that obtained for the fit of the Cr standards ($S_0^2 = 0.72$). The best fits were achieved with Cr in an octahedral environment of Se atoms. The fit with a single Cr–Se scattering path of Cr in an octahedral symmetry was slightly worse (higher misfit and reduced χ^2) and the σ^2 values larger (suggesting a dispersion of bond distances) than that performed with two different Cr-Se bonds. Thus the latter was considered the best fit, and the values of the structural parameters obtained from it are listed in Table II. It is worth mentioning that attempts to fit the coordination number for these paths were consistent with the octahedral symmetry found for the Cr atoms. In addition, other attempts revealed no contribution of Cr–Cr scattering paths, which rules out the presence of Cr clusters. Both XANES and EXAFS at the Cr K edge showed no clear Cr–O oxygen environment.

The EXAFS analysis indicates that the Cr dopants occupy octahedral sites, similar to Cr-doped Ga_2Se_3 dilute magnetic semiconductor [18] and the *ab initio* calculated Cr-doped Bi_2Se_3(111) surface [45]. In the latter study, a favorable configuration of substitutional Cr on the Bi sites of the Bi_2Se_3 lattice was found, with Cr-Se distances remarkably close to those we obtained by EXAFS (see Table II). This result indicates that the Cr atoms in the doped Bi_2Se_3 system are substitutional on the Bi sites, in which case the Se atoms need to contract locally towards the Cr compared to the original Bi–Se distance ($\Delta d \approx -0.36$ Å). GGA calculations for the structural relaxation predicted that the Se neighbors move towards the dopant by $\Delta d = -0.305$ Å and -0.362 Å for Se*1* and Se*2*, respectively [15]. This contraction strengthens the hybridization between the Cr and neighboring Se and thus the impurity bands broaden [24]. This GGA calculation further showed that band gap of Cr doped Bi_2Se_3 without relaxation is 0.28 eV, while after structural relaxation the band gap is reduced to 0.01 eV. GGA + U calculations and inclusion of the spin-orbit coupling give essentially the same result as GGA [15].

TABLE II. Structural parameters obtained from Cr K edge EXAFS fits for the Cr-doped Bi_2Se_3 thin film shown in Fig. 3(b). Coordination number, N, interatomic distance, R, and Debye-Waller factor, σ^2, for each path. A value of $\Delta E_0 = 1.5 \pm 0.3$ eV was obtained from the fit.

	Cr–Se*1*	Cr–Se*2*
N	3	3
R (Å)	2.53 ± 0.01	2.64 ± 0.01
σ^2 (Å^2)	0.003 ± 0.001	0.003 ± 0.001

B. Cr $L_{2,3}$ XAS and XMCD

Depth dependence. Since XAS is a surface sensitive technique we first consider its depth dependence. While total-electron yield (TEY) in normal incidence probes only the top 3–5 nm near the surface, fluorescence yield (FY) probes the entire 100 nm film, including part of the sapphire substrate. However, different selection rules, self-absorption, and saturation effects mean that the FY is not linearly proportional to the x-ray absorption, e.g., the L_2/L_3 peak intensity ratio is strongly enhanced in FY [32]. Therefore, FY should only be used in a qualitative manner, and applying the sum rules in this case can give a large error. TEY, on the other hand, is directly proportional to the x-ray absorption, with negligible saturation effects for diluted samples.

Figure 4 shows the Cr $L_{2,3}$ XAS spectra of doped Bi_2Se_3 measured in TEY and FY. The TEY was obtained in normal incidence and the FY in grazing incidence to reduce saturation effects. The L_3 edge in the TEY spectrum reveals two distinct peaks separated by 1.35 eV. The high-energy peak is notably absent in the FY spectrum, which means this peak originates from the top layers. Subtracting the FY spectrum from the TEY spectrum gives an indication of the nature of the surface contribution. For comparison the Cr_2O_3 standard measured in FY is shown in Fig. 4. The agreement with the difference spectrum in both spectral shape and energy position (~578 eV) confirms that the top layers contain mainly Cr^{3+}. This is further confirmed by comparing in Fig. 4 the XMCD measured by TEY and FY in 7 T field at 5 K. The XMCD (TEY) shows additional shoulders at the energy position of the Cr^{3+} $L_{2,3}$ peaks (indicated by arrows in Fig. 4). What does this mean for the assignment of the bulk peak? As a general rule, a more electropositive ion gives a peak at higher photon energy [27]. Thus this means that the bulk peak (at ~576 eV), which is at lower energy than the Cr^{3+} peak, must have more Cr^{2+} character.

XAS branching ratio. The branching ratio B is defined as the fraction of the total XAS intensity in the L_3 edge, i.e., $B = I(L_3)/[I(L_3) + I(L_2)]$. It has been shown that for high-spin states in octahedral crystal-field symmetry the value of B increases with the number of 3d electrons [59]. Multiplet calculations for octahedral crystal-field symmetry ($10Dq = 1.5$ eV) give $B = 0.593$ for Cr^{3+} $3d^3$ and $B = 0.672$ for Cr^{2+} $3d^4$. The measured Cr $L_{2,3}$ XAS in TEY of the TI has a branching ratio of 0.657, which indicates the presence of a large amount of Cr^{2+}. However, the branching ratio is also sensitive to the hybridization, so that a quantitative analysis would not be justified.

We note that the measured branching ratio can be assumed to be isotropic since the linear dichroism plays no significant

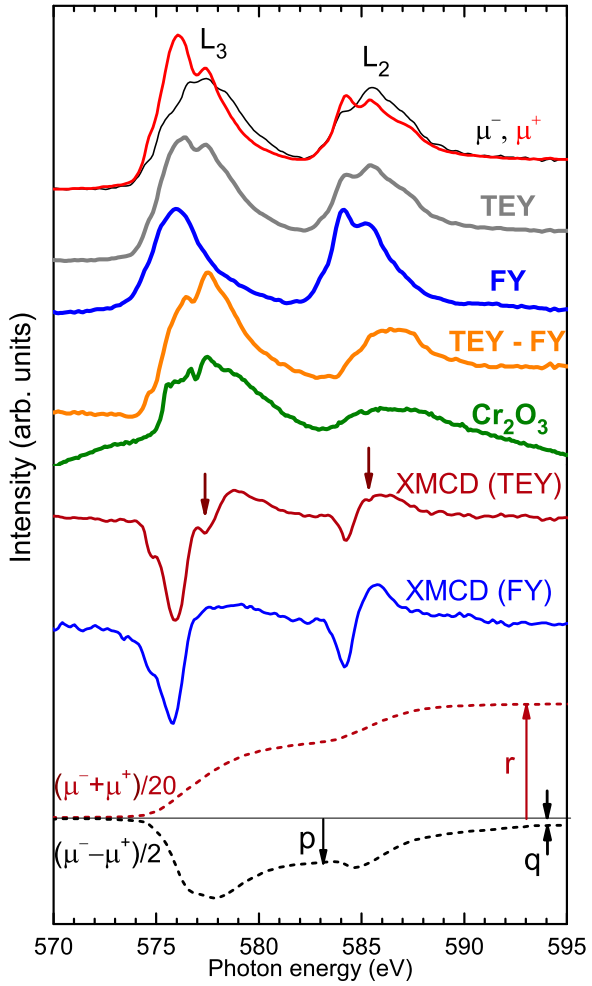

FIG. 4. (Color online) Experimental Cr $L_{2,3}$ XAS and XMCD spectra of Cr-doped Bi_2Se_3 and Cr_2O_3 reference in 7 T field at 5 K. From top to bottom: TEY spectra for opposite circular polarizations (μ^-, μ^+) in normal incidence, XAS averaged over the two polarizations for TEY in normal incidence and for FY in grazing incidence. Difference between the TEY and TY spectra for the Cr-doped Bi_2Se_3 is compared with the Cr_2O_3 reference measured in FY. XMCD spectra measured in TEY and FY. The arrows indicate additional shoulders at each edge in the XMCD (TEY) due to Cr^{3+}. Spectra are vertically offset for clarity. At the bottom, the dashed curves show the integrated intensities of the summed XAS ($\mu^- + \mu^+$) and the XMCD ($\mu^- - \mu^+$) measured in TEY. Values of p, q, and r appearing in the sum rules of Eq. (1) are indicated.

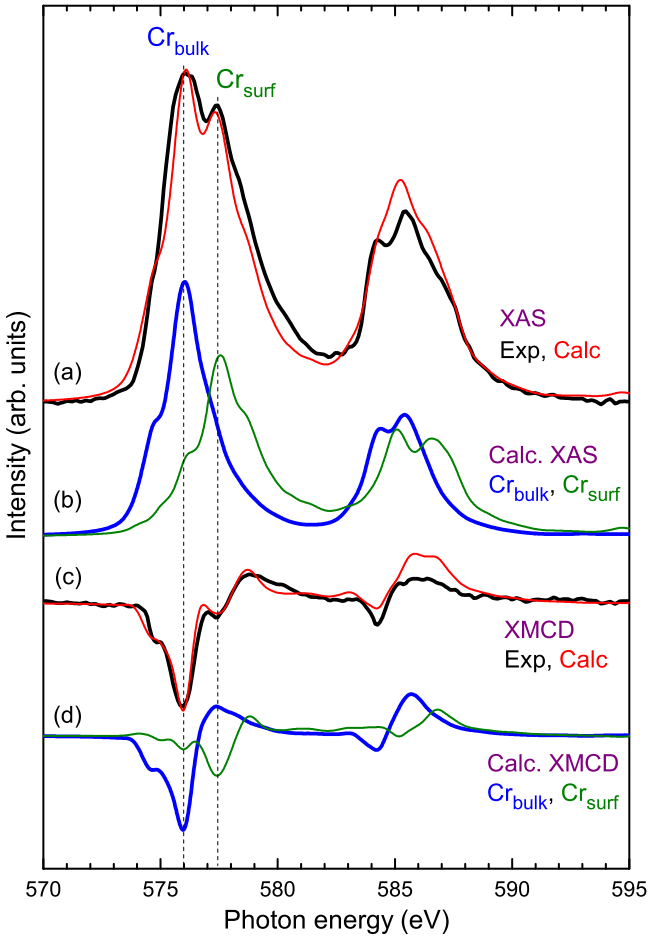

FIG. 5. (Color online) Cr $L_{2,3}$ spectra of Cr-doped Bi_2Se_3 in 7 T field at 5 K in TEY. (a) Comparison between calculated (Calc) and experimental (Exp) XAS spectrum ($\mu^- + \mu^+$). The latter is corrected for background steps at the L_3 and L_2 edges. (b) Separate contributions of Cr_{bulk} and Cr_{surf} to the calculated XAS. (c) Comparison between calculated and experimental XMCD spectrum ($\mu^- - \mu^+$). (d) Separate Cr_{bulk} and Cr_{surf} contributions to the calculated XMCD.

role in the case of 3*d* metals. If the symmetry is lower than cubic, there is a charge-quadrupole moment, which changes the total intensity of the linear dichroism but does not affect the branching ratio. According to the sum rules only ground-state operators containing a spin moment can change the branching ratio, namely the 3*d* spin-orbit interaction for the isotropic spectrum, the spin and magnetic-dipole operator for the XMCD, and the anisotropic spin-orbit interaction for the x-ray magnetic linear dichroism (XMLD), which is a small quantity [60–62].

Sum rule results. Applying the sum rules from Eq. (1) with a correction factor of $C = 2.0 \pm 0.2$ to the integrated intensities of the TEY spectra in Fig. 2(b) gives the average moments per Cr as $\mu_L = (0.04 \pm 0.1)\,\mu_B/Cr_{av}$ and $\mu_S = (2.90 \pm 0.3)\,\mu_B/Cr_{av}$, assuming that $\langle T_z \rangle$ can be neglected. According to the third Hund's rule for less than half-filled shell, μ_L should be negative, which is possible within the error bar. Since the orbital contribution is only a few percent, it does not significantly contribute to the total magnetic moment.

Fitting by multiplet calculations. Alternatively, the magnetic moment can be obtained by fitting experimental spectra with theoretical spectra. The measured spectra in Fig. 4 do not show a multiplet structure that is as distinct as for ionic Cr^{3+} [35,36], which suggests the *d* states are hybridized instead of atomiclike.

We will use mixed ground states to describe the Cr bulk and surface contributions, denoted as Cr_{bulk} and Cr_{surf}, which are predominantly divalent and trivalent, respectively (see Fig. 5). The ground state for Cr_{bulk} is taken as 70% d^4 and 30% d^3 in an octahedral crystal-field of $10Dq = 1.5$ eV, which gives $n = 3.7$ and $m_S = 2.89\,\mu_B/Cr_{bulk}$ atom. The ground state for Cr_{surf} is taken as 79% d^3 and 21% d^2 in an octahedral crystal field of

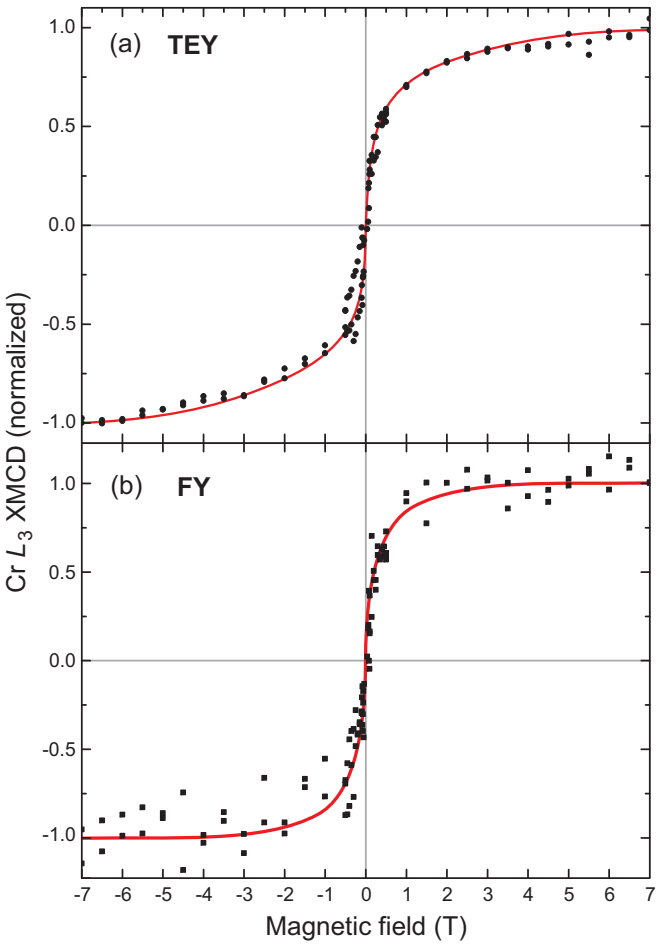

FIG. 6. (Color online) Hysteretic Cr L_3 XMCD at 5 K with the field applied normal to the sample up to ±7 T measured in (a) TEY and (b) FY. The red lines are guides for the eye.

$10Dq = 2$ eV, which gives $n = 2.78$ and $m_S = 2.83\,\mu_B/\mathrm{Cr_{surf}}$ atom. The choice of these two configurations is somewhat arbitrary, but this is not critical for the analysis. Also, in reality the octahedral symmetry is trigonally distorted to C_{3v} with three anions above and below it, which quenches the orbital moment but hardly affects the spin moment.

As shown in Fig. 5, the experimental XAS spectrum can be fitted with 0.54 $\mathrm{Cr_{bulk}} + 0.46$ $\mathrm{Cr_{surf}}$. Normalized to the total XAS, the measured XMCD is obtained with $0.68\,\mathrm{Cr_{bulk}} + 0.32\,\mathrm{Cr_{surf}}$, which corresponds to spin moments of $3.64\,\mu_B/\mathrm{Cr_{bulk}}$ and $1.91\,\mu_B/\mathrm{Cr_{surf}}$. As a check, this amounts to the average values of $n = 3.27$ and $m_S = 2.84\,\mu_B/\mathrm{Cr_{av}}$, in good agreement with the sum rule result $(2.90 \pm 0.3)\,\mu_B/\mathrm{Cr_{av}}$. Thus the multiplet analysis shows that the magnetic moment of $\mathrm{Cr_{bulk}}$ is almost saturated, and also that $\mathrm{Cr_{surf}}$ has a substantial magnetic moment. As observed by Vobornik *et al.* [63], in magnetically doped TIs the valence states near the surface can have very different properties than in the bulk. In our case, however, we cannot exclude a surface contribution caused by exposure to air.

XMCD hysteresis curve. Sweeping the applied field at the photon energy of the Cr L_3 peak gives an XMCD hysteresis loop, which reveals the field-dependent magnetization of the Cr moments. Figure 6(a) shows the surface-sensitive TEY and (b) the bulk-sensitive FY for positive helicity under normal incidence at 5 K. The TEY hysteresis loop (a) shows that the surface Cr moments saturate at the maximum field of 7 T. The FY hysteresis loop (b) shows the bulk Cr moments are saturating at ∼3 T. Both hysteresis loops show a ferromagnetic behavior, although no clear loop opening can be identified, which can be attributed to the remaining remanent field of 10 mT inside the superconducting magnet.

V. CONCLUSIONS

We have performed x-ray absorption studies at the Cr K and $L_{2,3}$ edges of epitaxially grown $Cr_{4.6}Bi_{35.4}Se_{60.0}$ thin films of high crystalline quality, which are free from secondary phases. We found that the Cr dopants substitute for Bi and are primarily divalent, with the key results summarized below. (i) Compared with various relevant standard samples, the energy position of the absorption jump for the Cr K edge in the doped Bi_2Se_3 thin film is close to that of CrSe, which has a valence of Cr^{2+}. (ii) The measured branching ratio of the Cr $L_{2,3}$ XAS is close to the calculated value for Cr^{2+}, and much different from that of Cr^{3+}. (iii) Comparing the Cr $L_{2,3}$ absorption spectra measured in FY and TEY detection with a Cr_2O_3 standard indicates that the surface peak is mainly Cr^{3+}, whereas the bulk peak is at lower photon energy. From the general rule that the peaks of more electropositive ions are found at higher photon energy [27], it follows that the bulk dopants must be more 2+. (iv) The XMCD sum rule analysis at the Cr $L_{2,3}$ measured in TEY, which contains both bulk and surface contributions, gives $\mu_S = (2.90 \pm 0.3)\,\mu_B/\mathrm{Cr_{av}}$. (v) Fitting the XAS and XMCD of the bulk and surface contributions separately, using multiplet calculations including charge transfer, gives spin moments of $3.64\,\mu_B/\mathrm{Cr_{bulk}}$ and $1.91\,\mu_B/\mathrm{Cr_{surf}}$, with an average spin moment of $2.84\,\mu_B/\mathrm{Cr_{av}}$ that is in agreement with the sum rule result. Hence the moment of $\mathrm{Cr_{bulk}}$ is almost fully saturated.

The analyses of the K-edge EXAFS and $L_{2,3}$ multiplet structure indicate that the Cr dopants occupy octahedral sites, similar to Cr-doped Ga_2Se_3 dilute magnetic semiconductor [18] and *ab initio* calculated Cr-doped Bi_2Se_3(111) surfaces [45]. In the latter study, a favorable configuration of Cr being substitutional on Bi sites of the Bi_2Se_3 lattice was found, with Cr–Se distances remarkably close to those we have obtained by EXAFS. This is also in good agreement with recent GGA(+U) calculations [15]. The result indicates that the Cr dopants in the Bi_2Se_3 system are substitutional on the Bi sites, in which case the Se atoms need to contract locally ($\Delta d \approx -0.36$ Å) toward the Cr atoms from their undisturbed Bi–Se distance.

We ascribe the Cr^{2+} character to the hybridization between the Cr $d(e_g)$ and Se p bands, which are located just above and below the Fermi level, respectively. This hybridization gives the observed smoothening of the $L_{2,3}$ multiplet structure. The mixing between the electronic states is increased by the rearrangement of the Se neighbors around the Cr site, as evidenced by the EXAFS analysis. Since the electronic charge is redistributed within the Cr–Se bonds, it does not contribute to the concentration of free carriers.

The Cr K-edge EXAFS results rule out the presence of Cr^0 and Cr–Cr bonds as expected for Cr clusters, which indicates

that Cr is well distributed in the Bi_2Se_3 matrix. Furthermore, Cr–O bonds are not evident in the Cr K-edge EXAFS results, given that this technique is less surface sensitive than the TEY-detected Cr $L_{2,3}$-edge XAS.

Our results will encourage a reevaluation of the assumptions made for the oxidation state of transition metal dopants in topological insulators. It will also give a stimulus to the initiation of theoretical calculations for the covalent bonding of the magnetic dopant with the neighboring Se or Te ions. Gaining a deeper understanding of the magnetic behavior of such topological insulators will allow for increasing the Curie temperature, thereby paving the way for low-power electronic applications in the future.

ACKNOWLEDGMENTS

We thank Diamond Light Source for beamtime awarded on I10 (BLADE) and rapid access on B18. We would like to thank R. Boada and D. Gianolio for their help. We also acknowledge the John Fell Oxford University Press (OUP) Research Fund.

[1] D. C. Grauer, Y. S. Hor, A. J. Williams, and R. J. Cava, Mater. Res. Bull. **44**, 1926 (2009).
[2] M. Z. Hasan and C. L. Kane, Rev. Mod. Phys. **82**, 3045 (2010).
[3] C. Corkhill, R. A. F. Ixer, J. S. Mason, D. Irving, and R. A. D. Pattrick, Scot. J. Geol. **46**, 23 (2010).
[4] R. J. Cava, H. Ji, M. K. Fuccillo, Q. D. Gibson, and Y. S. Hor, J. Mater. Chem. C **1**, 3176 (2013).
[5] L. He, X. Kou, and K. L. Wang, Phys. Status Solidi–Rapid Res. Lett. **7**, 50 (2013).
[6] J. J. Cha, K. J. Koski, and Y. Cui, Phys. Status Solidi–Rapid Res. Lett. **7**, 15 (2013).
[7] R. Yu, W. Zhang, H.-J. Zhang, S.-C. Zhang, X. Dai, and Z. Fang, Science **329**, 61 (2010).
[8] X.-L. Qi, T. L. Hughes, and S.-C. Zhang, Phys. Rev. B **78**, 195424 (2008).
[9] Y. L. Chen, J.-H. Chu, J. G. Analytis, Z. K. Liu, K. Igarashi, H.-H. Kuo, X. L. Qi, S. K. Mo, R. G. Moore, D. H. Lu, M. Hashimoto, T. Sasagawa, S. C. Zhang, I. R. Fisher, Z. Hussain, and Z. X. Shen, Science **329**, 659 (2010).
[10] L. A. Wray, S.-Y. Xu, Y. Xia, D. Hsieh, A. V. Fedorov, Y. S. Hor, R. J. Cava, A. Bansil, H. Lin, and M. Z. Hasan, Nat. Phys. **7**, 32 (2011).
[11] C.-Z. Chang, J. Zhang, X. Feng, J. Shen, Z. Zhang, M. Guo, K. Li, Y. Ou, P. Wei, L.-L. Wang, Z.-Q. Ji, Y. Feng, S. Ji, X. Chen, J. Jia, X. Dai, Z. Fang, S.-C. Zhang, K. He, Y. Wang, L. Lu, X.-C. Ma, and Q.-K. Xue, Science **340**, 167 (2013).
[12] J. Wang, B. Lian, H. Zhang, Y. Xu, and S.-C. Zhang, Phys. Rev. Lett. **111**, 136801 (2013).
[13] M. D. Watson, L. J. Collins-McIntyre, L. R. Shelford, A. I. Coldea, D. Prabhakaran, S. C. Speller, T. Mousavi, C. R. M. Grovenor, Z. Salman, S. R. Giblin, G. van der Laan, and T. Hesjedal, New J. Phys. **15**, 103016 (2013).
[14] V. A. Kulbachinskii, A. Y. Kaminskii, K. Kindo, Y. Narumi, K. Suga, P. Lošt'ák, and P. Svanda, Physica B **311**, 292 (2002).
[15] J.-M. Zhang, W. Ming, Z. Huang, G.-B. Liu, X. Kou, Y. Fan, K. L. Wang, and Y. Yao, Phys. Rev. B **88**, 235131 (2013).
[16] J.-M. Zhang, W. Zhu, Y. Zhang, D. Xiao, and Y. Yao, Phys. Rev. Lett. **109**, 266405 (2012).
[17] P. Larson and W. R. L. Lambrecht, Phys. Rev. B **78**, 195207 (2008).
[18] E. N. Yitamben, T. C. Lovejoy, A. B. Pakhomov, S. M. Heald, E. Negusse, D. Arena, F. S. Ohuchi, and M. A. Olmstead, Phys. Rev. B **83**, 045203 (2011).
[19] P. P. J. Haazen, J.-B. Laloë, T. J. Nummy, H. J. M. Swagten, P. Jarillo-Herrero, D. Heiman, and J. S. Moodera, Appl. Phys. Lett. **100**, 082404 (2012).
[20] X. F. Kou, W. J. Jiang, M. R. Lang, F. X. Xiu, L. He, Y. Wang, Y. Wang, X. X. Yu, A. V. Fedorov, P. Zhang, and K. L. Wang, J. Appl. Phys. **112**, 063912 (2012).
[21] H. Li, Y. R. Song, M. Yao, F. Yang, L. Miao, F. Zhu, C. Liu, C. L. Gao, D. Qian, X. Yao, J.-F. Jia, Y. Shi, and D. Wu, Appl. Phys. Lett. **101**, 072406 (2012).
[22] X. Kou, M. Lang, Y. Fan, Y. Jiang, T. Nie, J. Zhang, W. Jiang, Y. Wang, Y. Yao, L. He, and K. L. Wang, ACS Nano **7**, 9205 (2013).
[23] C.-Z. Chang, P. Tang, Y.-L. Wang, X. Feng, K. Li, Z. Zhang, Y. Wang, L.-L. Wang, X. Chen, C. Liu, W. Duan, K. He, X.-C. Ma, and Q.-K. Xue, Phys. Rev. Lett. **112**, 056801 (2014).
[24] J.-M. Zhang, W. Zhu, Y. Zhang, D. Xiao, and Y. Yao, Phys. Rev. Lett. **109**, 266405 (2012).
[25] J. S. Dyck, Č. Drašar, P. Lošťák, and C. Uher, Phys. Rev. B **71**, 115214 (2005).
[26] L. J. Collins-McIntyre, S. E. Harrison, P. Schönherr, N.-J. Steinke, C. J. Kinane, T. R. Charlton, D. Alba-Venero, A. Pushp, A. J. Kellock, S. S. P. Parkin, J. S. Harris, S. Langridge, G. van der Laan, and T. Hesjedal, Eur. Phys. Lett. **107**, 57009 (2014).
[27] G. van der Laan and I. W. Kirkman, J. Phys.: Condens. Matter **4**, 4189 (1992).
[28] L. Chotorlishvili, A. Ernst, V. K. Dugaev, A. Komnik, M. G. Vergniory, E. V. Chulkov, and J. Berakdar, Phys. Rev. B **89**, 075103 (2014).
[29] R. D. Shannon, Acta Crystallogr. A **32**, 751 (1976).
[30] G. van der Laan and B. T. Thole, Phys. Rev. B **43**, 13401 (1991).
[31] G. van der Laan, J. Phys.: Conf. Ser. **430**, 012127 (2013).
[32] G. van der Laan and A. I. Figueroa, Coord. Chem. Rev. **277-278**, 95 (2014).
[33] B. T. Thole, P. Carra, F. Sette, and G. van der Laan, Phys. Rev. Lett. **68**, 1943 (1992).
[34] P. Carra, B. T. Thole, M. Altarelli, and X. Wang, Phys. Rev. Lett. **70**, 694 (1993).
[35] M. Mizumaki, A. Agui, Y. Saitoh, M. Nakazawa, and T. Matsushita, Surf. Rev. Lett. **09**, 849 (2002).
[36] N. D. Telling, V. S. Coker, R. S. Cutting, G. van der Laan, C. I. Pearce, R. A. D. Pattrick, E. Arenholz, and J. R. Lloyd, Appl. Phys. Lett. **95**, 163701 (2009).
[37] D. E. Crean, V. S. Coker, G. van der Laan, and J. R. Lloyd, Environ. Sci. Technol. **46**, 3352 (2012).
[38] A. Kimura, J. Matsuno, J. Okabayashi, A. Fujimori, T. Shishidou, E. Kulatov, and T. Kanomata, Phys. Rev. B **63**, 224420 (2001).
[39] K. Yaji, A. Kimura, M. Koyama, C. Hirai, H. Sato, K. Shimada, A. Tanaka, and M. Taniguchi, J. Appl. Phys. **97**, 10A316 (2005).

[40] Y. Yamazaki, T. Kataoka, V. R. Singh, A. Fujimori, F.-H. Chang, D.-J. Huang, H.-J. Lin, C. T. Chen, K. Ishikawa, K. Zhang, and S. Kuroda, J. Phys.: Condens. Matter **23**, 176002 (2011).
[41] L. Tichy and J. Horak, Phys. Rev. B **19**, 1126 (1979).
[42] V. A. Kulbachinskii, N. Miura, H. Nakagawa, H. Arimoto, T. Ikaida, P. Lošt'ák, and C. Drasar, Phys. Rev. B **59**, 15733 (1999).
[43] T. Jungwirth, J. Masek, K. Y. Wang, K. W. Edmonds, M. Sawicki, M. Polini, J. Sinova, A. H. MacDonald, R. P. Campion, L. X. Zhao, N. R. S. Farley, T. K. Johal, G. van der Laan, C. T. Foxon, and B. L. Gallagher, Phys. Rev. B **73**, 165205 (2006).
[44] T. Siegrist, P. Jost, H. Volker, M. Woda, P. Merkelbach, C. Schlockermann, and M. Wuttig, Nat. Mater. **10**, 202 (2011).
[45] L. B. Abdalla, L. Seixas, T. M. Schmidt, R. H. Miwa, and A. Fazzio, Phys. Rev. B **88**, 045312 (2013).
[46] T. Dietl, Semicond. Sci. Technol. **17**, 377 (2002).
[47] B. Li, Q. Fan, F. Ji, Z. Liu, H. Pan, and S. Qiao, Phys. Lett. A **377**, 1925 (2013).
[48] B. Ravel and M. Newville, J. Synchrotron Radiat. **12**, 537 (2005).
[49] B. Ravel, J. Synchrotron Radiat. **8**, 314 (2001).
[50] I. Vobornik, U. Manju, J. Fujii, F. Borgatti, P. Torelli, D. Krizmancic, Y. S. Hor, R. J. Cava, and G. Panaccione, Nano Lett. **11**, 4079 (2011).
[51] J. Honolka, A. A. Khajetoorians, V. Sessi, T. O. Wehling, S. Stepanow, J.-L. Mi, B. B. Iversen, T. Schlenk, J. Wiebe, N. B. Brookes, A. I. Lichtenstein, P. Hofmann, K. Kern, and R. Wiesendanger, Phys. Rev. Lett. **108**, 256811 (2012).
[52] L. R. Shelford, T. Hesjedal, L. Collins-McIntyre, S. S. Dhesi, F. Maccherozzi, and G. van der Laan, Phys. Rev. B **86**, 081304(R) (2012).
[53] S. E. Harrison, L. J. Collins-McIntyre, S. Li, A. A. Baker, L. R. Shelford, Y. Huo, A. Pushp, S. S. P. Parkin, J. S. Harris, E. Arenholz, G. van der Laan, and T. Hesjedal, J. Appl. Phys. **115**, 023904 (2014).
[54] B. T. Thole, G. van der Laan, J. C. Fuggle, G. A. Sawatzky, R. C. Karnatak, and J. M. Esteva, Phys. Rev. B **32**, 5107 (1985).
[55] G. van der Laan, Lect. Notes Phys. **697**, 143 (2006).
[56] R. D. Cowan, *The Theory of Atomic Structure and Spectra* (University of California Press, Berkeley, 1992).
[57] G. van der Laan, Phys. Rev. B **57**, 112 (1998).
[58] K. W. Edmonds, N. R. S. Farley, T. K. Johal, G. van der Laan, R. P. Campion, B. L. Gallagher, and C. T. Foxon, Phys. Rev. B **71**, 064418 (2005).
[59] B. T. Thole and G. van der Laan, Phys. Rev. B **38**, 3158 (1988).
[60] G. van der Laan, Phys. Rev. Lett. **82**, 640 (1999).
[61] G. van der Laan, Phys. Rev. B **55**, 8086 (1997).
[62] G. van der Laan, E. Arenholz, R. V. Chopdekar, and Y. Suzuki, Phys. Rev. B **77**, 064407 (2008).
[63] I. Vobornik, G. Panaccione, J. Fujii, Z.-H. Zhu, F. Offi, B. R. Salles, F. Borgatti, P. Torelli, J. P. Rueff, D. Ceolin, A. Artioli, M. Unnikrishnan, G. Levy, M. Marangolo, M. Eddrief, D. Krizmancic, H. Ji, A. Damascelli, G. van der Laan, R. G. Egdell, and R. J. Cava, J. Phys. Chem. C **118**, 12333 (2014).